2014

Zero-Reabsorption Doped-Nanocrystal Luminescent Solar Concentrators

Stephen R. McDowall, *Western Washington University*
Christian S. Erickson, *University of Washington*
Liam R Bradshaw, *Western Washington University*
John D. Gilbertson, *Western Washington University*
Daniel R. Gamelin, *University of Washington*, et al.

Zero-Reabsorption Doped-Nanocrystal Luminescent Solar Concentrators

Christian S. Erickson,[†] Liam R. Bradshaw,[‡] Stephen McDowall,[§] John D. Gilbertson,[†] Daniel R. Gamelin,[‡,*] and David L. Patrick[†,*]

[†]Department of Chemistry, Western Washington University, 516 High Street, Bellingham, Washington 98225, United States, [‡]Department of Chemistry, University of Washington, Seattle, Washington 98195-1700, United States, and [§]Mathematics Department, Western Washington University, 516 High Street, Bellingham, Washington 98225, United States

ABSTRACT Optical concentration can lower the cost of solar energy conversion by reducing photovoltaic cell area and increasing photovoltaic efficiency. Luminescent solar concentrators offer an attractive approach to combined spectral and spatial concentration of both specular and diffuse light without tracking, but they have been plagued by luminophore self-absorption losses when employed on practical size scales. Here, we introduce doped semiconductor nanocrystals as a new class of phosphors for use in luminescent solar concentrators. In proof-of-concept experiments, visibly transparent, ultraviolet-selective luminescent solar concentrators have been prepared using colloidal Mn^{2+}-doped ZnSe nanocrystals that show no luminescence reabsorption. Optical quantum efficiencies of 37% are measured, yielding a maximum projected energy concentration of ~6× and flux gain for a-Si photovoltaics of 15.6 in the large-area limit, for the first time bounded not by luminophore self-absorption but by the transparency of the waveguide itself. Future directions in the use of colloidal doped nanocrystals as robust, processable spectrum-shifting phosphors for luminescent solar concentration on the large scales required for practical application of this technology are discussed.

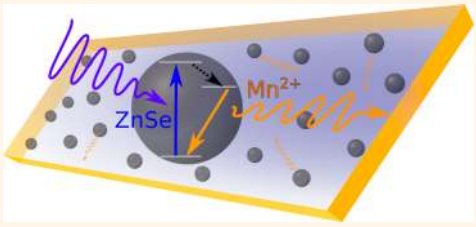

KEYWORDS: solar energy · solar concentrators · doped nanocrystals · transparent solar collector

Luminescent solar concentrators (LSCs) are dye-containing waveguides used to collect and concentrate sunlight for energy conversion.[1−3] Simultaneous spectral and spatial concentration is achieved without the use of focusing optics. Instead, sunlight absorbed by the dye is emitted into guided modes to travel by total internal reflection for collection at the perimeter (Figure 1). LSCs require no solar tracking, exhibit omnidirectional acceptance providing comparable performance under diffuse and specular illumination, and offer the potential for higher energy concentration ratios (CR) than designs based on mirrors or lenses.[4] Their ability to deliver high-irradiance, narrow-bandwidth light by active wavelength shifting makes LSCs particularly suitable for driving photovoltaics and semiconductor-based photochemical processes where wavelength-to-bandgap matching can be exploited to improve efficiency and mitigate thermal rejection.[5] Unlike lens- and mirror-based concentrators, LSCs selectively collect sunlight in a limited spectral band, established by the absorption range of the luminophore. Other wavelengths are transmitted for use in secondary applications such as interior lighting, heat generation, or photovoltaic conversion, enabling high combined-cycle efficiencies. The LSC itself obeys the single-bandgap Shockley−Queisser efficiency limit,[6] with maximum energy efficiencies of $E_{lim} \approx 3-5\%$ for UV-selective collection, increasing up to ~30% if absorption extends into the near-infrared. The thermodynamically limited energy concentration ratio depends on the effective luminescence Stokes shift, with values of $CR_{lim} \geq 100$ predicted at room temperature for a Stokes shift of ~0.1 eV.[7] Attached photovoltaics receive high-irradiance, narrow-bandwidth light, resulting in a power density enhancement (referred to as the flux gain) up to several times larger than CR_{lim} when the photovoltaic's bandgap is matched to luminophore emission.[8]

Despite several decades of research,[9,10] actual LSC performance levels remain far below these thermodynamic limits, primarily due to three main factors: (1) only a fraction of incident sunlight is absorbed,

* Address correspondence to david.patrick@wwu.edu, gamelin@chem.washington.edu.

Received for review December 11, 2013 and accepted March 12, 2014.

Published online 10.1021/nn406360w

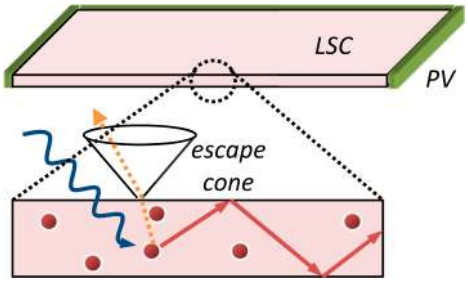

Figure 1. A luminescent solar concentrator. Sunlight (blue) is absorbed by luminophores and emitted into a planar waveguide (red), traveling to the edge of the collector to concentrate light for conversion by PV cells. A fraction of light is lost to nonunity LQY or out the escape cone (dashed orange) with each successive reabsorption/re-emission event.

determined by the integrated overlap of luminophore absorption and solar spectra; (2) only a fraction of absorbed light is re-emitted, depending on the luminophore's luminescence quantum yield (LQY); (3) only a fraction of this emitted light is captured in guided modes (~75% in an LSC waveguide with refractive index $n \sim 1.5$), with the remainder (~25%) lost out the top or bottom escape cone defined by Snell's Law.[11] Most problematic of all is that losses from mechanisms (2) and (3) occur repetitively, because photons traveling within the waveguide may be absorbed and re-emitted by other luminophores multiple times before reaching an edge. In practical LSC implementations, for example, optical path lengths may easily reach a meter or more, and even small overlap between absorption and emission spectra results in catastrophic self-absorption losses. Concentrator efficiencies thus fall exponentially with the number of reabsorption/re-emission events, which is in turn determined by the overlap of luminophore absorption and emission spectra and by the device dimensions.

Efforts to improve LSC performance by reducing luminophore self-absorption or mitigating its effects have included the use of dichroic mirrors and other photonic structures to reduce escape-cone losses,[12−15] controlling luminophore orientation to capture a greater proportion of emitted photons in guided modes,[16−20] and use of large Stokes shift luminophores.[21] Regarding the latter, a wide range of materials and strategies have been investigated, including organometallic and sensitized lanthanide phosphors,[22] Stokes shift enhancement by solid-state solvation,[23] and other concepts.[24−26] Various types of semiconductor nanocrystals (quantum dots, or QDs) have also been investigated, including those with both Type I and Type II heterointerfaces.[27,28] Despite these efforts, it has proven difficult to identify phosphors that simultaneously absorb strongly, are photostable, are solution processable, and generate sufficiently large Stokes shifts without sacrificing LQYs.

Here, we demonstrate a new class of LSCs based on impurity-doped QDs as the active phosphor material. Incorporation of small amounts (0.1−1 atom %) of a luminescence activator ion within a QD introduces new localized excited states within the bandgap that can be efficiently excited *via* exchange-mediated energy transfer from the photoexcited host semiconductor.[29] Emission from these states can be downshifted substantially relative to the semiconductor absorption so that, by choosing an activator whose extinction coefficient is sufficiently small, self-absorption can be effectively eliminated. The same mechanism is employed by classic sensitized inorganic phosphors commonly used in lighting or display applications.[30] Importantly, the small dimensions of colloidal doped QDs eliminates scattering effects typical of classic inorganic phosphor microcrystal powders.

In addition to minimal self-absorption and scattering, doped QDs possess several other characteristics useful for LSC applications. The semiconductor host provides a large extinction coefficient along with broadband absorption that is in principle tunable over a wide spectral range through composition and size control. Doped QDs also exhibit minimal concentration quenching and higher resistance to photo-oxidation than most organic dyes or undoped nanocrystals (due to rapid energy localization at the buried luminescence activator).[31] Depending on the semiconductor, they can be made from low cost, nontoxic, Earth-abundant starting materials, and they are compatible with a variety of economical solution-based synthesis and processing techniques advantageous for integration into polymer or glass waveguides. While doped QDs have been investigated extensively as phosphors[32−35] and for their unusual magneto-optical and magnetoelectronic properties,[36−39] to our knowledge this class of materials has not previously been used in LSCs.

As proof of concept, we have prepared and studied LSCs based on Mn^{2+}-doped ZnSe/ZnS core−shell quantum dots. The results presented here identify doped QDs as promising candidates for addressing the major challenges confronting the development of efficient LSCs. Although these challenges are not all fully overcome in the present study, our findings point to specific modifications of the doped QD compositions that could offer major improvements in device efficiency. Moreover, the specific doped QD materials described here may be of practical interest for unique applications ranging from window layers in stacked photovoltaics to transparent building-integrated energy-harnessing smart windows.

RESULTS AND DISCUSSION

ZnSe is a direct bandgap semiconductor with a bulk bandgap of ~3.1 eV, meaning it selectively absorbs UV light. In the weak tetrahedral field provided by the ZnSe lattice, substitutional Mn^{2+} impurity ions possess

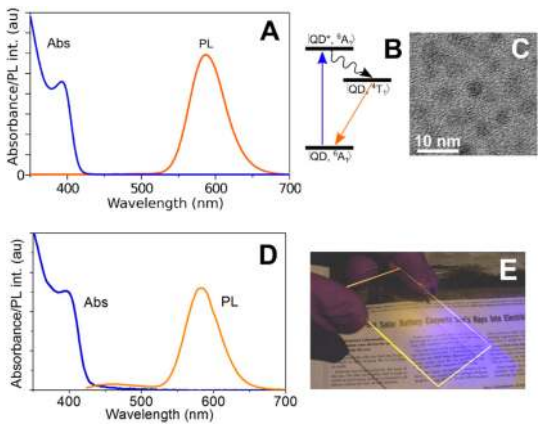

Figure 2. (A) Absorption and photoluminescence spectra of colloidal Mn^{2+}-doped ZnSe/ZnS QDs in toluene. (B) Schematic description of luminescence sensitization in Mn^{2+}-doped QDs. Photon absorption by the doped quantum dot in its ground state ($|QD,{}^6A_1\rangle$) gives the excited quantum dot ($|QD^*,{}^6A_1\rangle$). Energy rapidly localizes to excite Mn^{2+} within the QD ($|QD,{}^4T_1\rangle$), which then emits with a high quantum yield. Radiative processes are indicated as straight lines and nonradiative processes as wavy lines. (C) TEM image of representative Mn^{2+}-doped ZnSe/ZnS QDs. (D) Absorbance and photoluminescence spectra of Mn^{2+}:ZnSe/ZnS QDs in an LSC device. (E) A device seen under UV illumination.

a ${}^6A_1$ ground state and show luminescence associated with a ${}^4T_1 \rightarrow {}^6A_1$ $d-d$ transition at an energy of ~2.1 eV (Figure 2A).[29] This Mn^{2+} luminescence is efficiently sensitized by the host ZnSe nanocrystal (Figure 2B). The luminescence sensitization scheme active in our colloidal Mn^{2+}-doped ZnSe nanocrystals is very similar to that of bulk Mn^{2+}-doped ZnSe, but the colloids show greater sensitization efficiencies because of longer excitonic lifetimes and faster energy transfer. At room temperature, the rate of energy transfer from the photoexcited nanocrystal to Mn^{2+} (~ps) greatly exceeds that of exciton recombination (~ns),[40,41] making quantitative energy capture by Mn^{2+} possible. The excited Mn^{2+} then relaxes to its ground state with a high room-temperature LQY. The corresponding ${}^6A_1 \rightarrow {}^4T_1$ absorption transition is spin-forbidden, with a maximum extinction coefficient of only ~1 M^{-1} cm^{-1}, about 5 orders of magnitude smaller than that of the host nanocrystal. This difference in absorptivity yields a large *effective* Stokes shift of as much as ~1 eV, precluding self-absorption of Mn^{2+} emission and thereby overcoming a key challenge in LSC phosphor design. Although the long (~ms) lifetime of the ${}^4T_1$ excited state can lead to luminescence quenching *via* a multiphoton process,[41,42] the threshold photon flux for this effect greatly exceeds solar irradiance.[57]

Mn^{2+}-doped ZnSe/ZnS nanocrystals (Figure 2C) were synthesized by methods adapted from those described previously[41,43,44] and incorporated into polymer films by dispersing a toluene suspension of nanocrystals into a mixture of laurylmethacrylate, trioctyl phosphine, and ethylene glycol dimethacrylate, containing a photoinitiator (Methods). Devices were

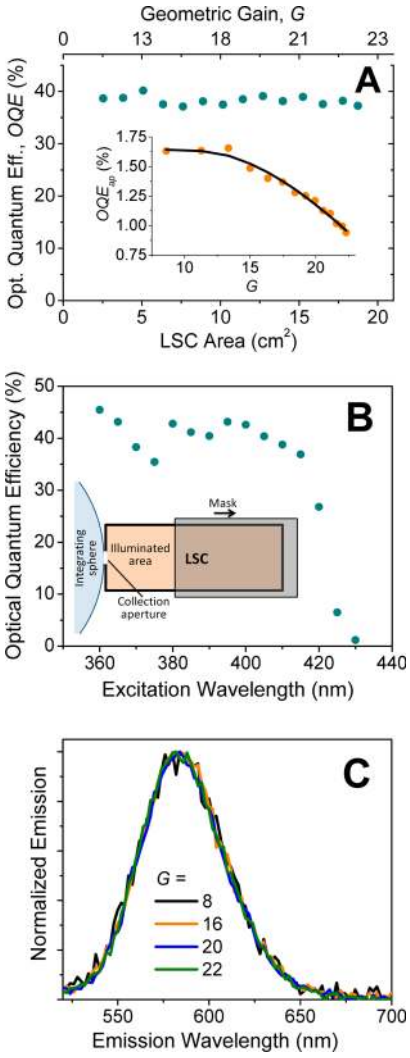

Figure 3. (A) The dependence of optical quantum efficiency on doped-nanocrystal LSC area and geometric gain for full perimeter, index-matched collection (OQE), and as measured through the collection aperture (OQE_{ap}, inset). Solid line results from fitting the model described in the text and SI. (B) Dependence of the OQE on excitation wavelength. OQE is independent of excitation wavelength above the bandgap. Inset: A monochromatic excitation source positioned above the device provides uniform light over the unmasked area, with edge-emitted light collected through an aperture into an integrating sphere. (C) Normalized edge emission spectra. (A) and (C) were obtained by excitation at 400 nm.

largely transparent to visible light (Figure 2E), with an optical density up to 0.30 at the first exciton absorption maximum, depending on the concentration of doped QDs used. Despite this transparency, waveguided luminescence is still clearly visible by eye when exposed to diffuse sunlight on a cloudy day (see Supporting Information (SI)). Overall concentrator dimensions were 25 × 75 × 0.42 mm, corresponding to a geometric gain, defined as the ratio of facial to edge area, $G = 22$.

LSC absorbance and facial emission spectra are shown in Figure 2D. The peak exciton absorption occurs at 396 nm and is size-tunable over the range 350–450 nm for this composition. The small

absorption tail extending from the band edge is likely caused by scattering. With above-bandgap excitation (400 nm), luminescence is dominated by the Mn^{2+} $^4T_1 \rightarrow {}^6A_1$ transition centered at 582 nm. A second broad emission feature is observed at ~435 nm that can be attributed to weak fluorescence from the waveguide polymer. This feature was also present in control devices containing no doped QDs, and it was not present in the toluene suspension of doped QDs.

Unlike other concentrator designs, wavelengths not collected by an LSC are transmitted and hence available for use by a secondary process, such as for interior lighting. Accordingly, LSC performance is expressed in terms of the fraction of solar photons harvested by the concentrator, or optical quantum efficiency (OQE), defined as the fraction of absorbed photons concentrated at device edges. OQE was measured as a function of geometric gain under uniform diffuse illumination by collecting edge-emitted light through an aperture into an integrating sphere connected to a fluorometer. The remaining device perimeter was blackened with ink to eliminate reflections. Successively larger illuminated areas were measured using a movable mask (inset, Figure 3B) and the full perimeter OQE was computed, correcting for the finite size of the edge collection aperture and reflection losses at the aperture arising from the use of a non-index-matched detector (for details, see SI). Figure 3A shows the results of these measurements under illumination near the first excitonic absorption peak (400 nm). OQE_{ap}, shown in the inset, is the non-index-matched collection efficiency through the small measurement aperture; the main figure shows the full perimeter OQE for an index-matched detector. The difference in curvature between the two plots stems from the decreasing solid angle occupied by the aperture as G increases. At $G = 22$, corresponding to full area illumination, OQE = 37%, with efficiency being independent of excitation energy above the bandgap (Figure 3B). As shown in Figure 3C, the spectral distribution of edge-emitted light shows negligible variation with increasing G, contrasting with the behavior of previously studied LSC luminophores where self-absorption produces a strong bathochromic shift in edge-emitted light with increasing G.[45] This result highlights the lack of self-absorption in doped nanocrystal LSCs.

In the absence of self-absorption, the relationship between OQE, luminophore LQY, and waveguide propagation and escape cone losses is

$$\mathrm{OQE} = \mathrm{LQY}\epsilon_{ec}\epsilon_{wg}(G) \quad (1)$$

where the escape cone loss term is given by Snell's Law, $\epsilon_{ec} = 1 - (1 - 1/n^2)^{1/2} \approx 0.75$, based on isotropic emission, and a waveguide refractive index $n = 1.5$. $\epsilon_{wg}(G)$ represents losses due to waveguide scattering and absorption, whose combined effects are expressed through a waveguide attenuation coefficient α_{dB}, defined such that the fraction of photons lost per unit distance l is $e^{-4.34l/\alpha_{dB}}$.[46] Given ϵ_{ec}, eq 1 allows determination of the other two loss mechanisms in an LSC, LQY and waveguide losses, from measurements of OQE *vs* G. For a uniformly illuminated rectangular LSC measuring $L \times W$, the proportion of emitted light surviving to reach an edge, subject to waveguide losses, is

$$\epsilon_{wg}(G) = \frac{1}{4\pi WL}\int_0^W \int_0^L \int_0^{2\pi} 2\int_{\theta_{ec}}^{\pi/2} e^{-4.34\alpha_{dB}l(x,y,\theta,\varphi)} \sin\theta \, d\theta \, d\varphi \, dy \, dx \quad (2)$$

where $\theta_{ec} = \sin^{-1}(1/n)$ is the escape cone angle, and $l(x, y, \theta, \varphi)$ is the distance a photon travels to the edge when emitted from (x, y) with directional spherical coordinates (θ, φ). Combining eqs 1 and 2 and solving numerically, we fit the measured $OQE_{ap}(G)$ (inset Figure 3A) to find LQY = 53% and $\alpha_{dB} = 0.085$ dB/cm (see SI for details). For the sample in Figure 3, the doped QD LQY measured in toluene was 50%, close to the fitted value. This result indicates that the doped QD LQY is preserved upon incorporation into the polymer device.

The flux gain,

$$F \approx \mathrm{CR}(\eta_{PV}^{e_{em}}/\eta_{PV}^{AM1.5}) \quad (3)$$

is the power produced from edge-attached photovoltaic cells relative to that produced from the same photovoltaic cells under direct AM1.5 exposure. Here $\eta_{PV}^{e_{em}}$ and $\eta_{PV}^{AM1.5}$ are the photovoltaic conversion efficiencies at the peak LSC emission energy and under broadband AM1.5 illumination, respectively, and the energy concentration ratio CR = OQE × $GN_{abs}e_{em}$, where N_{abs} is the number of solar photons absorbed by the LSC per unit area per second, found by integrating the AM1.5 solar spectrum over the doped QD absorption range (300−420 nm, Figure 3B), and $e_{em} = 2.12$ eV is the energy per luminescent photon. Figure 4 shows the size-dependent energy concentration ratio for a square LSC based on the LQY and α_{dB} for the experimental device in Figure 3, as well as the flux gain predicted for attached a-Si photovoltaic cells (see SI for details). The maximum concentration ratio and power density enhancement are projected to reach $CR_{max} = 6\times$ and $F_{max} = 15.6\times$ in the large-G limit, among the highest yet reported.[20,23,47−49] Projected maximum flux gains for other benchmark photovoltaic technologies are given in Table S1 (SI); several

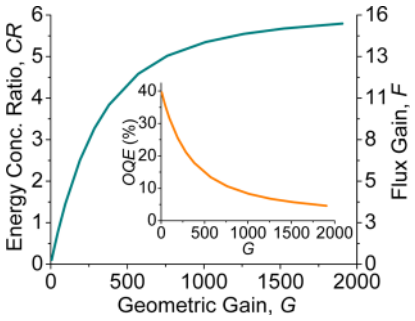

Figure 4. Predicted energy concentration ratio and flux gain for a-Si PVs as a function of geometric gain for square Mn^{2+}-doped ZnSe/ZnS nanocrystal LSCs (α_{dB} = 0.085 dB/cm, LQY = 0.53). *F* and CR asymptotically approach 15.6× and 6× in the large area limit, respectively. Inset: optical quantum efficiency becomes limited by parasitic waveguide losses at large *G*. For our device thickness, *G* = 2000 corresponds to an LSC edge length of 3.36 m. See SI for details.

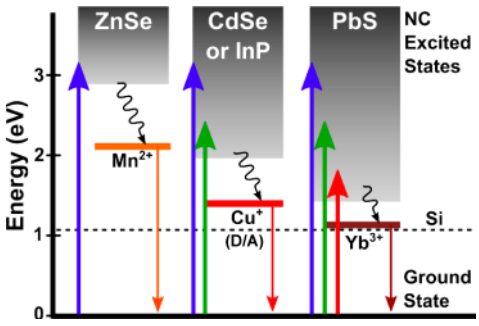

Figure 5. Potential dopant/semiconductor materials combinations for doped-nanocrystal-based LSCs. Cu^{+}-doped CdSe or InP nanocrystals show donor/acceptor recombination luminescence that is red-shifted from the semiconductor absorption edge. Yb^{3+}-doped PbS is anticipated to show sharp sensitized Yb^{3+} *f*–*f* luminescence. These and related doped nanocrystals would improve LSC performance by harvesting a broader portion of the solar spectrum and providing better luminescence matching with Si photovoltaics, while retaining the small reabsorption losses displayed by Mn^{2+}-doped ZnSe nanocrystals.

exceed 10×. These findings demonstrate the potential to achieve substantial reductions in photovoltaic area through optical concentration using doped nanocrystal LSCs. CR_{max} and F_{max} in doped QD LSCs are limited by parasitic waveguide losses (α_{dB}), which become the dominant loss mechanism for large *G* (inset, Figure 4). Such losses affect all LSCs, but heretofore have generally been negligible compared to self-absorption related losses. This result suggests that significant further improvements in large-area doped QD concentrator performance should be possible using more transparent polymer waveguide materials, for example, optical polysiloxanes or cyclic perfluoropolymers, which have intrinsic attenuation coefficients 1–3 orders of magnitude lower than polyacrylates at visible and near-IR wavelengths.[50,51] Importantly, the fact that competitive F_{max} values can be achieved by pairing Si photovoltaics with a phosphor that absorbs little of the solar spectrum illustrates the pivotal importance of eliminating reabsorption losses.

CONCLUSIONS

In summary, colloidal doped nanocrystals are demonstrated as a promising new class of zero-reabsorption luminophores for LSC applications. Using Mn^{2+}-doped ZnSe/ZnS nanocrystals as the active phosphor material, concentrating polymer films capable of selectively absorbing solar UV light and producing intensified emission with optical quantum efficiencies approaching 40% have been demonstrated. These concentrators are largely transparent to visible light, making them attractive for application as transparent window coatings or in multijunction concentrator/PV configurations. As the first report of this approach, we anticipate further major improvements in LSC efficiencies using doped semiconductor nanocrystals. For the Mn^{2+}-doped ZnSe/ZnS-based LSCs described here, the nanocrystal LQYs can be increased by optimizing QD surface passivation, and the energy gap can be narrowed by alloying with a small amount of Cd^{2+}. Waveguide losses, currently the limiting factor in our devices, can be reduced by improved processing and use of more transparent polymers. As such, the Mn^{2+}-doped nanocrystal LSCs described here hold promise for practical window-layer applications where transparency is desired. Restricting absorption to UV wavelengths limits the collectable fraction of sunlight to less than 10% of total irradiance, so transparent concentrators based on these materials would produce less power per unit area than many conventional PV panels. More generally, even higher LSC limiting efficiencies, concentration ratios, and flux gains can be expected from the use of related doped nanocrystals that absorb and emit at lower energies.

Although it is not yet clear which doped nanocrystals will perform best in aggregate, two specific targets are proposed on the basis of their anticipated absorption and luminescence properties (Figure 5). First, replacing ZnSe with CdSe or InP would allow extension of the nanocrystal absorption down to as low as the ~1.3 eV InP bulk bandgap (~950 nm). Doping semiconductor nanocrystals with Cu^{+} typically gives rise to donor–acceptor luminescence whose maximum is shifted by ~0.5 eV from the first absorption maximum, with little reabsorption. Both Cu^{+}-doped CdSe and Cu^{+}-doped InP nanocrystals have been synthesized previously,[52,53] but they have not yet been thoroughly explored, and in particular they have not yet been examined as phosphors for LSCs. Even further improvement could be achieved by doping PbS nanocrystals with Yb^{3+} ions, which should show sharp *f*–*f* luminescence centered at ~1.2 eV (~1000 nm), well matched with the Si energy gap. Yb^{3+}-doped PbS nanocrystals of appropriate diameter could absorb near this energy, again with negligible reabsorption

losses. Colloidal Yb^{3+}-doped PbS nanocrystals have not been made, and in fact represent a major synthetic challenge,[54−56] but the experimental LSC results presented here indicate they are worthy targets. Efforts to develop these and related doped nanocrystals for application in LSCs are presently underway.

METHODS

Doped QD Synthesis. Mn^{2+}-doped ZnSe core nanocrystals were prepared by lyothermal degradation of $[Zn_4(SePh)_{10}](Me_4N)_2$ in the presence of $MnCl_2$. ZnS shells were grown by successive ionic layer adsorption and reaction (SILAR) deposition from $Zn(oleate)_2$ and tri-*n*-octyl phosphine sulfide (TOP-S). In a typical synthesis, 200 mg of $[Zn_4(SePh)_{10}](Me_4N)_2$ and 10 mg of Se were added anaerobically to a degassed mixture of 5.4 g of hexadecylamine and 5 mg of $MnCl_2$ in a three-necked round-bottom flask, and the temperature was raised to 275 °C. After 20−60 min at 275 °C, the mixture was cooled and nanocrystals precipitated by addition of ethanol. The nanocrystals were then resuspended in toluene, where they were purified by repeated precipitation with ethanol, isolation by centrifuging, and resuspension in toluene. Following purification, ZnS shells were grown by alternating slow addition of approximately monolayer equivalents of $Zn(oleate)_2$ and TOP-S to a degassed mixture containing the isolated nanocrystals, 1.5 g of oleylamine, and 1.5 g of octadecene, held at 225 °C. Each addition was allowed to react for 30 min before the subsequent addition. After shell growth, the mixture was cooled and purified in the same manner as described above. Electronic absorption spectra of toluene suspensions were collected using a Cary 500 spectrometer. Photoluminescence spectra were collected using 405 nm excitation and an Ocean Optics USB2000 spectrometer for detection. Transmission electron microscopy (TEM) images were collected using a FEI Tecnai G2 F20.

Device Fabrication. Nanocrystals were incorporated into polymer films by dispersing a toluene suspension into a 5:1:1 by weight mixture of laurylmethacrylate, trioctyl phosphine, and ethylene glycol dimethacrylate, containing <1 wt % of Irgacure 651 photoinitiator (CIBA). Several droplets of the resulting mixture were placed onto a clean borosilicate glass coverslip, which was then covered by a second coverslip, and the resulting glass/solution/glass samples were photopolymerized with UV light under nitrogen for 1−3 h to form a solid film with a thickness of approximately 100 μm. Except at the collection aperture, all device edges were blackened with a marker.

Device Characterization. Absorbance measurements were performed with a Jasco UV−vis spectrophotometer. Edge emission measurements were performed using a Horiba Fluorolog model FL3-21 fluorometer connected *via* fiber optic cable to an integrating sphere. Further details are provided in the text and SI.

Conflict of Interest: The authors declare no competing financial interest.

Acknowledgment. This work was supported by the National Science Foundation through DMR-1035512 (S.M., J.D.G., and D.L.P.) and DMR-1206221 (D.R.G.). Part of this work was conducted at the University of Washington NanoTech User Facility, a member of the NSF National Nanotechnology Infrastructure Network (NNIN). The authors wish to thank Tyler Suronen for his assistance in performing geometric calculations, and Dr. Emily McLaurin for her assistance in the preparation of doped QDs.

Supporting Information Available: Derivation of the computation of full-perimeter OQE from measurements over a small aperture, projected maximum flux gains for benchmark photovoltaic technologies, photograph of a doped QD LSC in sunlight. This material is available free of charge *via* the Internet at http://pubs.acs.org.

REFERENCES AND NOTES

1. Weber, W. H.; Lambe, J. Luminescent Greenhouse Collector for Solar Radiation. *Appl. Opt.* **1976**, *15*, 2299–2300.
2. Goetzberger, A.; Greubel, W. Solar Energy Conversion with Fluorescent Collectors. *Appl. Phys.* **1977**, *14*, 123–139.
3. Swanson, R. M. The Promise of Concentrators. *Prog. Photovoltaics: Res. Appl.* **2000**, *8*, 93–111.
4. Debije, M. G.; Verbunt, P. P. C. Thirty Years of Luminescent Solar Concentrator Research: Solar Energy for the Built Environment. *Adv. Energy Mater.* **2012**, *2*, 12–35.
5. Huang, X.; Han, S.; Huang, W.; Liu, X. Enhancing Solar Cell Efficiency: the Search for Luminescent Materials as Spectral Converters. *Chem. Soc. Rev.* **2013**, *42*, 173–201.
6. Rau, U.; Einsele, F.; Glaeser, G. C. Efficiency Limits of Photovoltaic Fluorescent Collectors. *Appl. Phys. Lett.* **2005**, *87*, article no. 171101.
7. Smestad, G.; Ries, H.; Winston, R.; Yablonovitch, E. The Thermodynamic Limits of Light Concentrators. *Sol. Energy Mater.* **1990**, *21*, 99–111.
8. Batcheldar, J. S.; Zewail, A. H.; Cole, T. Luminescent solar concentrators. 1: Theory of Operation and Techniques for Performance Evaluation. *Appl. Opt.* **1979**, *18*, 3090–3110.
9. Verbunt, P. P. C.; Debije, M. G. Progress in Luminescent Solar Concentrator Research: Solar Energy for the Built Environment. In *Proceedings of the World Renewable Energy Congress*; Elsevier: Amsterdam, 2011; pp 2751−2759.
10. van Sark W. G. J. H. M. Luminescent Solar Concentrators—A Low Cost Photovoltaics Alternative. *2nd European Energy Conference*, Maastricht, The Netherlands, **2012**, EPJ Web of Conferences 33, 02003.
11. The critical angle of the escape cone is $\theta_c = \sin^{-1}(n_{clad}/n_{core})$, where n_{clad} and n_{core} are the refractive indices of the waveguide cladding and core. For a polymer or glass waveguide in air with n_{clad} = 1.5−1.7, this leads to θ_c = 35−45°, and η_{trap} = 0.7−0.8. Thus 20−30% of photons are lost with each successive reabsorption/re-emission.
12. Goldschmidt, J. C.; Peters, M.; Prönneke, L.; Steidl, L.; Zentel, R.; Bläsi, B.; Gombert, A.; Glunz, S.; Willeke, G.; Rau, U. Theoretical and Experimental Analysis of Photonic Structures for Fluorescent Concentrators with Increased Efficiencies. *Phys. Status Solidi* **2008**, *205*, 2811–2821.
13. Debije, M. G.; Van, M-P; Verbunt, P. P. C.; Kastelijn, M. J.; vander Blom, R. H. L.; Broer, D. J.; Bastiaansen, W. M. Effect on the Output of a Luminescent Solar Concentrator on Application of Organic Wavelength-Selective Mirrors. *Appl. Opt.* **2010**, *49*, 745–751.
14. Giebink, N. C.; Wiederrecht, G. P; Wasielewski, M. R. Resonance-shifting to Circumvent Reabsorption Loss in Luminescent Solar Concentrators. *Nat. Photonics* **2001**, *5*, 694–701.
15. Verbunt, P. P. C.; Broer, D. J.; Bastiaansen, C. W. M.; Debije, M. G. The Effect of an Organic Selectively-Reflecting Mirror on the Performance of a Luminescent Solar Concentrator. *Proceedings of the 24th European PV Solar Energy Conference*; WIP Wirtschaft und Infrastruktur GmbH & Co Planungs KG: Munich, 2009; pp 381−384.
16. Mulder, C. L.; Reusswig, P. D; Velázquez, A. M.; Kim, H.; Rotschild, C.; Baldo, M. A. Dye Alignment in Luminescent Solar Concentrators: I. Vertical Alignment for Improved Waveguide Coupling. *Opt. Express* **2010**, *18*, A79–A90.
17. Debije, M. G. Solar Energy Collectors with Tunable Transmission. *Adv. Funct. Mater.* **2010**, *20*, 1498–1502.
18. McDowall, S.; Butler, T.; Bain, E.; Scharnhorst, K.; Patrick, D. L. Comprehensive Analysis of Escape-Cone Losses from Luminescent Waveguides. *Appl. Opt.* **2013**, *52*, 1230–1239.
19. MacQueen, R. W.; Cheng, Y. Y.; Clady, R. G. C. R.; Schmidt, T. W. Towards an Aligned Luminophore Solar Concentrator. *Opt. Express* **2010**, *18*, A161–A166.
20. Benjamin, W. E.; Veit, D. R.; Perkins, M. J.; Bain, E.; Scharnhorst, K.; McDowall, S.; Patrick, D. L.; Gilbertson, J. D. Sterically Engineered Perylene Dyes for High Efficiency Oriented Fluorophore Luminescent Solar Concentrators. *Chem. Mater.* **2014**, *26*, 1291–1293.

21. Krumer, Z.; van Sark, G. J. H. M. W.; Donegá, C.; Schropp, R. E. I. Exploration of Parameters Influencing the Self-absorption Losses in Luminescent Solar Concentrators with an Experimentally Validated Combined Ray-tracing/Monte-Carlo Model. *Proc. SPIE* **2013**, *8821*, 882104. High and Low Concentrator Systems for Solar Electric Applications VIII.
22. De Boer, D. K. G.; Broer, D. J.; Debije, M. G.; Keur, W.; Meijerink, A.; Ronda, C. R.; Verbunt, P. P. C. Progress in Phosphors and Filters for Luminescent Solar Concentrators. *Opt. Express* **2012**, *20*, A395–A405.
23. Currie, M. J.; Mapel, J. K.; Heidel, T. D.; Goffri, S.; Baldo, M. A. High-Efficiency Organic Solar Concentrators for Photovoltaics. *Science* **2008**, *321*, 226–228.
24. Sanguineti, A.; Sassi, M.; Turrisi, R.; Ruffo, R.; Vaccaro, G.; Meinardi, F.; Beverina, L. High Stokes Shift Perylene Dyes for Luminescent Solar Concentrators. *Chem. Commun.* **2013**, *49*, 1618–1620.
25. van Sark, W. G. J. H. M.; Barnham, K. W. J.; Slooff, L. H.; Chatten, A. J.; Büchtemann, A.; Meyer, A.; McCormack, S. J.; Koole, R.; Farrell, D. J.; Bose, R.; *et al.* Luminescent Solar Concentrators—A Review of Recent Results. *Opt. Express* **2008**, *16*, 21773–21792.
26. Saraidarov, T.; Levchenko, V.; Grabowska, A.; Borowicz, P.; Reisfeld, R. Non-Self-Absorbing Materials for Luminescent Solar Concentrators (LSC). *Chem. Phys. Lett.* **2012**, *492*, 60–62.
27. Purcell-Milton, F.; Gun'ko, Y. K. J. Quantum Dots for Luminescent Solar Concentrators. *J. Mater. Chem.* **2012**, *22*, 16687–16697.
28. Kumer, Z.; Pera, S. J.; van Dijk-Moes, R. J. A.; Zhao, Y.; de Brouwer, A. F. P.; Groeneveld, E.; van Sark, W. G. J. H. M.; Schropp, R. E. I.; Donega, D. dM. Tackling Self-absorption in Luminescent Solar Concentrators with Type-II Colloidal Quantum Dots. *Sol. Energy Mater. Sol. Cells* **2013**, *111*, 57–65.
29. Beaulac, R.; Archer, P. I.; Gamelin, D. R. Luminescence in Colloidal Mn^{2+}-Doped Semiconductor Nanocrystals. *J. Solid State Chem.* **2008**, *181*, 1582–1589.
30. Ronda, C., Ed.; *Luminescence: From Theory to Applications*; Wiley-VCH: Weinheim, 2008.
31. Hyldahl, M. G.; Bailey, S. T.; Wittmershaus, B. P. Photostability and Performance of CdSe/ZnS Quantum Dots in Luminescent Solar Concentrators. *Sol. Energy* **2009**, *83*, 566–573.
32. Bol, A. A.; Meijerink, A. Long-lived Mn^{2+} Emission in Nanocrystalline ZnS:Mn^{2+}. *Phys. Rev. B: Condens. Matter Mater. Phys* **1998**, *58*, R15997–R16000.
33. Suyver, J. F.; Wuister, S. F.; Kelly, J. J.; Meijerink, A. Luminescence of Nanocrystalline ZnSe:Mn^{2+}. *Phys. Chem. Chem. Phys.* **2000**, *2*, 5445–5448.
34. Pradhan, N.; Battaglia, D. M.; Liu, Y.; Peng, X. Efficient, Stable, Small, and Water-Soluble Doped ZnSe Nanocrystal Emitters as Non-Cadmium Biomedical Labels. *Nano Lett.* **2007**, *7*, 312–317.
35. Sarkar, S.; Karan, N. S.; Pradhan, N. Ultra-Small Color Tunable Cu Doped Ternary Nanocrystal Emitters. *Angew. Chem., Int. Ed.* **2011**, *50*, 6065–6069.
36. Hoffman, D. M.; Meyer, B. K.; Ekimov, A. I.; Merkulov, I. A.; Efros, A. L.; Rosen, M.; Couino, G.; Gacoin, T.; Boilot, J. P. Giant Internal Magnetic Fields in Mn Doped Nanocrystal Quantum Dots. *Solid State Commun.* **2000**, *114*, 547–550.
37. Norris, D. J.; Yao, N.; Charnock, F. T.; Kennedy, T. A. High-Quality Manganese-Doped ZnSe Nanocrystals. *Nano Lett.* **2001**, *1*, 3–7.
38. Beaulac, R.; Archer, P. I.; Liu, X.; Lee, S.; Salley, G. M.; Dobrowolska, M.; Furdyna, J. K.; Gamelin, D. R. Spin-Polarizable Excitonic Luminescence in Colloidal Mn^{2+}-Doped CdSe Quantum Dots. *Nano Lett.* **2008**, *8*, 1197–1201.
39. Beaulac, R.; Schneider, L.; Archer, P. I.; Bacher, G.; Gamelin, D. R. Light-Induced Spontaneous Magnetization in Doped Colloidal Quantum Dots. *Science* **2009**, *325*, 973–976.
40. Chen, H. Y.; Chen, T. Y.; Son, D. H. Measurement of Energy Transfer Time in Colloidal Mn-Doped Semiconductor Nanocrystals. *J. Phys. Chem. C* **2010**, *114*, 4418–4423.
41. Bradshaw, L. R.; Hauser, A.; McLaurin, E. J.; Gamelin, D. R. Luminescence Saturation *via* Mn^{2+}-Exciton Cross Relaxation in Colloidal Doped Semiconductor Nanocrystals. *J. Phys. Chem. C* **2012**, *116*, 9300–9310.
42. Irvine, S. E.; Staudt, T.; Rittweger, E.; Engelhardt, J.; Hell, S. W. Direct Light-Driven Modulation of Luminescence from Mn-Doped ZnSe Quantum Dots. *Angew. Chem., Int. Ed.* **2008**, *47*, 2516–2519.
43. McLaurin, E. J.; Vlaskin, V. A.; Gamelin, D. R. Water-Soluble Dual-Emitting Nanocrystals for Ratiometric Optical Thermometry. *J. Am. Chem. Soc.* **2011**, *133*, 14978–14980.
44. Reiss, P.; Protière, M.; Li, L. Core/Shell Semiconductor Nanocrystals. *Small* **2009**, *5*, 154–168.
45. Wilson, L. R.; Rowan, B. C.; Robertson, N.; Moudam, O.; Jones, A. C.; Richards, B. S. Characterization and Reduction of Reabsorption Losses in Luminescent Solar Concentrators. *Appl. Opt.* **2010**, *49*, 1651–1661.
46. Thomas, M. E. Optical Propagation. In *Linear Media: Atmospheric Gases and Particles, Solid-State Components, and Water*; Oxford University Press: New York, 2006.
47. Mugnier, J.; Dordet, Y.; Pouget, J.; Valeur, B. A Photometric Approach of Fluorescent Solar Concentrators. Role of Diffuse Reflectors and Spectral Sensitivity of Solar Cells. *Rev. Phys. Appl.* **1987**, *22*, 89–99.
48. Roncali, J.; Garnier, F. Photon-Transport Properties of Luminescent Solar Concentrators: Analysis and Optimization. *Appl. Opt.* **1984**, *23*, 2809–2817.
49. Batcheldar, J. S.; Zewail, A. H.; Cole, T. Luminescent Solar Concentrators. 2: Experimental and Theoretical Analysis of Their Possible Efficiencies. *Appl. Opt.* **1981**, *20*, 3733–3754.
50. Su, K.; DeGroot, J. V., Jr.; Norris, A. W.; Lo, P. Y. Siloxane Materials for Optical Applications. *Proc. SPIE* **2005**, *6029*, 60291C.
51. Kirsch, P. *Modern Fluoroorganic Chemistry*; Wiley-VCH: Weinheim, 2013.
52. Meulenberg, R. W.; van Buuren, T.; Hanif, K. M.; Willey, T. M.; Strouse, G. F.; Terminello, L. J. Structure and Composition of Cu-Doped CdSe Nanocrystals Using Soft X-ray Absorption Spectroscopy. *Nano Lett.* **2004**, *4*, 2277–2285.
53. Xie, R.; Peng, X. Synthesis of Cu-Doped InP Nanocrystals (d-dots) with ZnSe Diffusion Barrier as Efficient and Color-Tunable NIR Emitters. *J. Am. Chem. Soc.* **2009**, *131*, 10645–10651.
54. Beaulac, R.; Ochsenbein, S. T.; Gamelin, D. R. Colloidal Transition-Metal-Doped Quantum Dots. In *Nanocrystal Quantum Dots*, 2nd ed.; Klimov, V. I., Ed.; CRC Press: Boca Raton, FL, 2010; pp 397−453.
55. Martín-Rodríguez, R.; Geitenbeek, R.; Meijerink, A. Incorporation and Luminescence of Yb^{3+} in CdSe Nanocrystals. *J. Am. Chem. Soc.* **2013**, *135*, 13668–13671.
56. Vlaskin, V. A.; Barrows, C. J.; Erickson, C. S.; Gamelin, D. R. Nanocrystal Diffusion Doping. *J. Am. Chem. Soc.* **2013**, *135*, 14380–14389.
57. Under broadband solar illumination the threshold for two photon quenching is reached roughly when the arrival rate per nanocrystal of absorbable photons (*i.e.*, those with energies exceeding ϵ_{abs}) approaches the turnover frequency ($\sim 10^4$ s^{-1}). The integrated AM1.5G photon flux from 280 to 425 nm (corresponding approximately the doped QD absorption range) is 10^{16} photons cm^{-2} s^{-1}. Assuming a doped QD extinction coefficient 10^5 M^{-1} cm^{-1} and a concentration high enough to absorb 99% of incident sunlight up to ϵ_{abs} (10^{-7} mol cm^{-2}), the quenching onset threshold is approximately 10^3 Suns.

Zero-Reabsorption Doped-Nanocrystal Luminescent Solar Concentrators

Christian S. Erickson[1], Liam R. Bradshaw[2], Stephen McDowall[3], John D. Gilbertson[1], Daniel R. Gamelin[2,*], David L. Patrick[1,*]

[1]Department of Chemistry, Western Washington University, 516 High St., Bellingham, WA, 98225
[2]Department of Chemistry, University of Washington, Seattle, WA 98195-1700
[3]Mathematics Department, Western Washington University, 516 High St., Bellingham, WA, 98225

Supporting Information

Determination of the optical quantum efficiency. The measured experimental data, $OQE_{ap}(L)$, consist of non-index-matched collection of light over an aperture of width A centered on the $W = 2.5\ cm$ edge of an LSC with lateral dimensions $L \times W\ cm^2$; the LSC is illuminated uniformly over the full top face. From these measurements, we wish to estimate what would be the $OQE_{full}(L)$ of an LSC with lateral dimensions $L \times W\ cm^2$ if photons were collected on all four edges by an index-matched collection device. Computation of this estimate is based on the assumption that a photon which has been absorbed and emitted by a QD will not undergo a second absorption. We do, however, wish to include the possibility of loss of photons due to scattering and extinction by the matrix itself. Assuming that the probability of such loss is independent of location within the LSC, this loss is described by an extinction coefficient α. In what follows, we describe how we determine both LQY and α from the measured data.

Let $OQE^*_{ap}(L\,;\alpha,Q)$ be the theoretical measurement we will calculate, taking into account the Fresnel relations at the measurement aperture and assuming a matrix extinction of α and LQY of Q. By fitting $OQE^*_{ap}(L_j\,;\alpha,Q)$ to $OQE_{ap}(L_j)$ for the lengths L_j for which we have measurements, we determine α^* and Q^*, the best-fit parameters. Both $OQE_{ap}(L)$ and $OQE^*_{ap}(L\,;\alpha,Q)$ assume non-index-matched measurements. From knowledge of α^* and Q^* we can then compute $OQE^*_{full}(L)$, the predicted measurement when collection is made on all edges of the LSC and measurement is index-matched.

We introduce lateral coordinates (x,y) so that the LSC is $-W/2 \le x \le W/2, 0 \le y \le L$, and the aperture is $-A/2 \le x \le A/2, y = 0$. (The thickness of the LSC plays no role in these computations.) To obtain OQE^*_{ap}, let $p(x,y\,;\alpha,Q)$ be the probability that a photon emitted from position (x,y) in the LSC: (i) reaches the side $y = 0$ within the aperture, at any z-value; (ii) lies within the side escape cone of the aperture; and (iii) refracts out of the LSC. Allowing z to be unconstrained corresponds to allowing

total internal reflection between the top and bottom faces. The third requirement takes into account the transmission coefficient for unpolarized light, determined from the Fresnel relations. Given $p(x, y\,; \alpha, Q)$ (which is derived below), we have

$$OQE^*_{ap}(L\,; \alpha, Q) = \frac{1}{LW}\int_{-W/2}^{W/2}\int_0^L p(x, y\,; \alpha, Q)\, dx\, dy.$$

To obtain $p(x, y\,; \alpha, Q)$, first let $-\pi < \phi_1(x, y) < \phi_2(x, y) < 0$ be such that the directions $(\cos\phi_i, \sin\phi_i)$ from (x, y) meet $(-W/2, 0)$ and $(W/2, 0)$, respectively. For each $\phi_1(x, y) < \phi < \phi_2(x, y)$, we define $0 \le \theta\big(\phi(x, y)\big) \le \pi/2$ by

$$\theta\big(\phi(x, y)\big) = \begin{cases} \sin^{-1}\left(\dfrac{-1}{\sin\phi(x, y)}\sqrt{1 - \dfrac{1}{n^2}}\right), & 1 - \dfrac{1}{n^2} < \sin^2\phi(x, y) \\ 1, & \text{otherwise.} \end{cases}$$

This definition is such that either the vector $\vec{v}(\theta, \phi) = (\sin\theta\cos\phi, \sin\theta\sin\phi, \cos\theta)$ lies within the side escape cone (centered on the normal vector $\vec{v} = (0, -1, 0)$ to the aperture) precisely for $\theta\big(\phi(x, y)\big) \le \theta \le \pi/2$, or $\theta\big(\phi(x, y)\big) = \pi/2$ if there is no θ for which the direction with that ϕ lies within the side escape cone. We define the transmission coefficient $T = 1 - \frac{1}{2}(R_s + R_p)$ where

$$R_s^2 = \begin{cases} \dfrac{n\,\vec{v}\cdot\vec{\nu} - \sqrt{1 - n^2(\vec{v}\cdot\vec{\nu})^2}}{n\,\vec{v}\cdot\vec{\nu} + \sqrt{1 - n^2(\vec{v}\cdot\vec{\nu})^2}}, & \vec{v}\cdot\vec{\nu} > \sin^{-1}\dfrac{1}{n}, \\ 1, & \text{otherwise,} \end{cases}$$

$$R_p^2 = \begin{cases} \dfrac{n\sqrt{1 - n^2(\vec{v}\cdot\vec{\nu})^2} - \vec{v}\cdot\vec{\nu}}{n\sqrt{1 - n^2(\vec{v}\cdot\vec{\nu})^2} + \vec{v}\cdot\vec{\nu}}, & \vec{v}\cdot\vec{\nu} > \sin^{-1}\dfrac{1}{n}, \\ 1, & \text{otherwise.} \end{cases}$$

Define T as a function of (θ, ϕ) by way of $\vec{v}(\theta, \phi)$ given in spherical coordinates. With these definitions,

$$p(x, y\,; \alpha, Q) = \frac{Q}{4\pi}\int_{\phi_1(x,y)}^{\phi_2(x,y)} 2\int_{\theta(\phi(x,y))}^{\pi/2} T(\theta, \phi)\exp(-\alpha l(x, y, \theta, \phi))\sin\theta\, d\theta\, d\phi,$$

where $l(x, y, \theta, \phi)$ is the distance from the point (x, y) to the edge $y = 0$ in the direction with spherical coordinates (θ, ϕ). Specifically, $l(x, y, \theta, \phi) = \frac{-y}{\sin\theta \sin\phi}$.

Because α is unknown, we cannot compute $OQE^*_{ap}(L\,; \alpha, Q)$ directly. However, for values of $\alpha\, l \ll 1$, $\exp(-\alpha l) = 1 - \alpha l + \frac{1}{2}(\alpha l)^2 - \frac{1}{6}(\alpha l)^3 + \cdots \approx \sum_{j=0}^{N} \frac{\alpha^j l^j}{j!}$. As we shall see below, the requirement that $\alpha\, l \ll 1$ does indeed hold and the approximation is accurate with N as low as 3 or 4. We define the α-independent and Q-independent functions, $i \geq 0$,

$$f_i(L) = \frac{1}{2\pi LW} \int_{-W/2}^{W/2} \int_0^L \int_{\phi_1(x,y)}^{\phi_2(x,y)} \int_{\theta(\phi(x,y))}^{\pi/2} T(\theta, \phi) l(x, y, \theta, \phi)^i \sin\theta \; d\theta \; d\phi \; dx \; dy$$

which we can numerically compute for the measurement lengths $L_1, \ldots, L_{14}$ ($W = 2.5$). We then have

$$OQE^*_{ap}(L_k\,; \alpha, Q) \approx Q\left(f_0 - \alpha f_1(L_k) + \frac{1}{2}\alpha^2 f_2(L_k) - \cdots + \frac{(-1)^N}{N!}\alpha^N f_N(L_k) \right).$$

For a given N, we can now minimize the mean squared error (MSE) between this vector of values and the measured values:

$$\{\alpha^*, Q^*\} = \text{argmin}\left\{ \sum_{k=0}^{14} \left(OQE^*_{ap}(L_k; \alpha, Q) - OQE_{ap}(L_k) \right)^2 \right\}.$$

We find that MSE is 1.6×10^{-6} even for $N = 0$, but drops to 1.1×10^{-6} for $N = 3$ and remains so for $N = 4, 5$; the values of $\alpha^* = 0.0195$ and $Q^* = 0.530$ also remain unchanged beyond $N = 3$. In the paper we report the attenuation coefficient in units of dB / cm, computed from α^* using $\alpha_{dB} = 10\alpha^* \log_{10} e = 0.085$, where e is Euler's number.

Using α^*, Q^*, we can now calculate $OQE^*_{full}(L, W)$. Extend the definition of $l(x, y, \theta, \phi)$ to be the distance from (x, y) to the appropriate edge met by the vector with spherical coordinates (θ, ϕ). Then

$$OQE^*_{full}(L, W) = \frac{Q^*}{2\pi LW} \int_{-W/2}^{W/2} \int_0^L \int_0^{2\pi} \int_{\theta(\phi(x,y))}^{\pi/2} \exp(-\alpha^*\, l(x, y, \theta, \phi)) \sin\theta \; d\theta \; d\phi \; dx \; dy.$$

In particular, we compute $OQE^*_{full}(L_k, 2.5)$ to obtain the predicted full perimeter, index-matched OQE measurements. In the main part of Figure 2A we plot $OQE_{ap}(L)\frac{OQE^*_{full}(L)}{OQE^*_{ap}(L)}$. We can further compute $OQE^*_{full}(L, L)$ for increasingly large values of L to predict performance of larger square LSCs (Figure 4).

Table S1. Projected maximum flux gains for Mn^{2+}-doped ZnSe/ZnS nanocrystal LSCs coupled to benchmark photovoltaic technologies, based on the experimental LSC parameters.

PV technology	Ref.	$\eta_{PV}^{AM1.5}$ (%)	$\eta_{PV}^{e_{em}}$ (%)	F_{max}
CIGS[(a)]	1	19.6	25.8	7.9
GaAs[(b)]	2	28.8	44.4	9.3
CdTe[(c)]	3	18.3	28.9	9.5
DSSC[(d)]	4	11.0	21.8	11.9
a-Si[(e)]	5	10.1	26.0	15.6
polymer[(f)]	11	9.9	26.2	15.9

[(a)]$CuInGaSe_2$ (National Renewable Energy Laboratory), *EQE* = 0.97, V_{OC} = 0.71 V, *FF* = 0.79. [(b)]Thin film GaAs (Alta Inc.), *EQE* = 0.97, V_{OC} = 1.12 V, *FF* = 0.87. [(c)]CdTe (General Electric, Inc.) *EQE* = 0.93, V_{OC} = 0.86 V, *FF* = 0.77. [(d)]Dye sensitized solar cell (Sharp Inc.) *EQE* = 0.92, V_{OC} = 0.71 V, *FF* = 0.70. [(e)]Amorphous silicon (Oerliken Solar), *EQE* = 0.93, V_{OC} = 0.89 V, *FF* = 0.67. [(f)]Polymer (Konarka Inc.), *EQE* = 0.97, V_{OC} = 0.82 V, *FF* = 0.70. Neglecting coupling losses and based on CR_{lim} = 6. V_{OC} does not include enhancements resulting from concentration, and hence may underestimate the maximum flux gain. *EQE* = photovoltaic external quantum efficiency at 2.12 eV; V_{OC} = open circuit voltage; *FF* = fill factor. Reported values at 25° C under AM1.5 conditions. $\eta_{PV}^{e_{em}} = (EQE \times V_{OC} \times FF)/(Ce_{em})$, C is the electronic charge.

Figure S1. A Mn^{2+}-doped ZnSe/ZnS nanocrystal luminescent solar concentrator device under diffuse solar excitation (cloudy day). Although largely transparent to visible light, the orange wave-guided luminescence of Mn^{2+} is clearly seen at the device edges.

1 Green, M. A; Emery, K.; Hishikawa, Y.; Warta, W; Solar Cell Efficiency Tables (Version 37). *Prog. Photovolt: Res. Appl*. **2011** 19, 84-92.

2 Green, M. A; Emery, K.; Hishikawa, Y.; Warta, W; Dunlop E.D.; Solar Cell Efficiency Tables (Version 40). *Prog. Photovolt: Res. Appl*. **2012** 20, 606-614.

3 Green, M. A; Emery, K.; Hishikawa, Y.; Warta, W; Dunlop E.D.; Solar Cell Efficiency Tables (Version 41). *Prog. Photovolt: Res. Appl*. **2013** 21, 1-11.

4 Green, M. A; Emery, K.; Hishikawa, Y.; Warta, W; Dunlop E.D.; Solar Cell Efficiency Tables (Version 39). *Prog. Photovolt: Res. Appl*. **2011** 20, 12-20.

5 Green, M. A; Emery, K.; Hishikawa, Y.; Warta, W; Solar Cell Efficiency Tables (Version 36). *Prog. Photovolt: Res. Appl*. **2010** 18, 346-352.